

# Relativistic mean-field description of nuclei at the drip-lines

D. Vretenar<sup>1,2</sup>, P. Ring<sup>2</sup>, and G.A. Lalazissis<sup>2</sup>

<sup>1</sup> Physics Department, Faculty of Science, University of Zagreb, Croatia

<sup>2</sup> Physik-Department der Technischen Universität München, D-85748 Garching, Germany

**Abstract.** We present a review of recent applications of the relativistic mean-field theory to the structure of nuclei close to the drip-lines. For systems with extreme isospin values, the relativistic Hartree-Bogoliubov model provides a unified and self-consistent description of mean-field and pairing correlations. The model has been applied in studies of structure phenomena that include: formation of neutron skin and of neutron halos in light nuclei in the mass region above the s-d neutron shell, the strong isospin dependence of the effective spin-orbit interaction and the resulting modification of surface properties, the suppression of the spherical  $N = 28$  shell gap for neutron-rich nuclei and the related phenomenon of deformation and shape coexistence, the proton drip-line in the spherical nuclei  $14 \leq Z \leq 28$ , and ground-state proton radioactivity in the region of deformed nuclei  $59 \leq Z \leq 69$ .

## INTRODUCTION

Experimental and theoretical studies of exotic nuclei with extreme isospin values present one of the most active areas of research in nuclear physics. Experiments with radioactive nuclear beams provide the opportunity to study very short-lived nuclei with very large neutron to proton ratios  $N/Z$ . New theoretical models and techniques are being developed in order to describe unique phenomena in nuclei very different from those usually encountered along the line of stability. On the neutron-rich side in particular, exotic phenomena include the weak binding of the outermost neutrons, pronounced effects of the coupling between bound states and the particle continuum, regions of nuclei with very diffuse neutron densities, formation of the neutron skin and halo structures. The modification of the effective nuclear potential produces a suppression of shell effects, the disappearance of spherical magic numbers, and the onset of deformation and shape coexistence. Isovector quadrupole deformations are expected at the neutron drip-lines, and possible low-energy collective isovector modes have been predicted. Because of their relevance to the r-process in nucleosynthesis, nuclei close to the neutron drip-line are also very important in nuclear astrophysics. Their properties determine the astrophysical conditions for the formation of neutron-rich stable isotopes.

Proton-rich nuclei also display many interesting structure phenomena which are important both for nuclear physics and astrophysics. These nuclei are characterized by exotic ground-state decay modes such as direct emission of charged particles and  $\beta$ -decays with large Q-values. The properties of many proton-rich nuclei should also play an important role in the process of nucleosynthesis by rapid-proton capture. In addition to decay properties (particle emission,  $\beta$ -decay), of fundamental importance are studies of atomic masses and separation energies, and especially the precise location of proton drip-lines.

Particularly important are nuclear systems with an equal number of proton and neutrons. Due to the high symmetry between the proton and neutron degrees of freedom, it is possible to study the details of the effective off-shell  $n - p$  interaction. Protons and neutrons occupy the same shell-model orbitals and therefore these nuclei present unique systems in which  $(S = 0, T = 1)$  and  $(S = 1, T = 0)$  pairing can be studied. While for  $A \leq 40$  the  $N = Z$  nuclei are  $\beta$ -stable, in heavier systems the Coulomb interaction drives the beta-stability line towards neutron-rich isotopes. Heavier  $N = Z$  nuclei approach the proton drip-line and display a variety of structure phenomena: shape coexistence, superdeformation, alignment of proton-neutron pairs, proton radioactivity from highly excited states.

Some of the most interesting examples of nuclear systems with large isospin values are provided by the recent experimental results on the synthesis and stability of the heaviest elements. The periodic system has been extended with three new elements  $Z = 110, 111, 112$ . These elements are found beyond the macroscopic limit of nuclear stability and are stabilized only by quantal shell effects. All the heaviest elements found recently are believed to

be well deformed. Still heavier and more neutron-rich elements are expected to be spherical and stabilized by shell effects, which strongly influence the spontaneous fission and alpha-decay half-lives.

While an impressive amount of experimental data on properties of exotic nuclei has been published in the last decade, the development of theoretical models has proceeded at a somewhat slower pace. Significant progress has been reported in the development of mean-field theories and theoretical models which use effective interactions to describe low energy nuclear states. Calculations based on modern Monte Carlo shell-model techniques provide a relatively accurate description of the structure of light and medium-mass exotic nuclei. For medium-heavy and heavy systems the only viable approach at present are large scale self-consistent mean-field calculations (Hartree-Fock, Hartree-Fock-Bogoliubov, relativistic mean-field). However, the present accuracy of model predictions, in general, is not comparable with the precision of modern experimental research facilities, and there are many serious technical difficulties in the calculation of properties of complex nuclear systems at the drip-lines.

Models based on quantum hadrodynamics [1] provide a framework in which the nuclear system is described by interacting baryons and mesons. In comparison with conventional non relativistic descriptions, relativistic models explicitly include mesonic degrees of freedom and consider the nucleons as Dirac particles. A variety of nuclear phenomena have been described in the relativistic framework: nuclear matter, properties of finite spherical and deformed nuclei, hypernuclei, neutron stars, nucleon-nucleus and electron-nucleus scattering, relativistic heavy-ion collisions. In particular, relativistic models based on the mean-field approximation have been successfully applied in the description of properties of spherical and deformed  $\beta$ -stable nuclei, and more recently in studies of exotic nuclei far from the valley of beta stability.

## THE RELATIVISTIC HARTREE-BOGOLIUBOV MODEL

Detailed properties of nuclear matter and of finite nuclei along the  $\beta$ -stability line have been very successfully described with relativistic mean-field models [2]. The nucleus is described as a system of Dirac nucleons, which interact in a relativistic covariant manner through the exchange of virtual mesons: the isoscalar scalar  $\sigma$ -meson, the isoscalar vector  $\omega$ -meson and the isovector vector  $\rho$ -meson. The effective Lagrangian density of quantum hadrodynamics reads

$$\begin{aligned} \mathcal{L} = & \bar{\psi} (i\gamma \cdot \partial - m) \psi \\ & + \frac{1}{2}(\partial\sigma)^2 - U(\sigma) - \frac{1}{4}\Omega_{\mu\nu}\Omega^{\mu\nu} + \frac{1}{2}m_\omega^2\omega^2 - \frac{1}{4}\vec{R}_{\mu\nu}\vec{R}^{\mu\nu} + \frac{1}{2}m_\rho^2\rho^2 - \frac{1}{4}F_{\mu\nu}F^{\mu\nu} \\ & - g_\sigma\bar{\psi}\sigma\psi - g_\omega\bar{\psi}\gamma \cdot \omega\psi - g_\rho\bar{\psi}\gamma \cdot \rho\tau\psi - e\bar{\psi}\gamma \cdot A\frac{(1-\tau_3)}{2}\psi. \end{aligned} \quad (1)$$

Vectors in isospin space are denoted by arrows, and bold-faced symbols will indicate vectors in ordinary three-dimensional space. The Dirac spinor  $\psi$  denotes the nucleon with mass  $m$ .  $m_\sigma$ ,  $m_\omega$ , and  $m_\rho$  are the masses of the  $\sigma$ -meson, the  $\omega$ -meson, and the  $\rho$ -meson.  $g_\sigma$ ,  $g_\omega$ , and  $g_\rho$  are the corresponding coupling constants for the mesons to the nucleon.  $e^2/4\pi = 1/137.036$ . The coupling constants and unknown meson masses are parameters, adjusted to fit data of nuclear matter and of finite nuclei.  $U(\sigma)$  denotes the non-linear  $\sigma$  self-interaction

$$U(\sigma) = \frac{1}{2}m_\sigma^2\sigma^2 + \frac{1}{3}g_2\sigma^3 + \frac{1}{4}g_3\sigma^4, \quad (2)$$

and  $\Omega^{\mu\nu}$ ,  $\vec{R}^{\mu\nu}$ , and  $F^{\mu\nu}$  are field tensors

$$\Omega^{\mu\nu} = \partial^\mu\omega^\nu - \partial^\nu\omega^\mu \quad (3)$$

$$\vec{R}^{\mu\nu} = \partial^\mu\vec{\rho}^\nu - \partial^\nu\vec{\rho}^\mu \quad (4)$$

$$F^{\mu\nu} = \partial^\mu A^\nu - \partial^\nu A^\mu. \quad (5)$$

The lowest order of the quantum field theory is the *mean-field* approximation: the meson field operators are replaced by their expectation values. The  $A$  nucleons, described by a Slater determinant  $|\Phi\rangle$  of single-particle spinors  $\psi_i$ , ( $i = 1, 2, \dots, A$ ), move independently in the classical meson fields. The sources of the meson fields are defined by the nucleon densities and currents. The ground state of a nucleus is described by the stationary self-consistent solution of the coupled system of Dirac and Klein-Gordon equations. Due to time reversal invariance, there are no currents in the static solution for an even-even system, and therefore the spatial vector components  $\omega$ ,  $\rho_3$  and  $\mathbf{A}$  of the vector meson fields vanish. The Dirac equation reads

$$\left\{ -i\boldsymbol{\alpha} \cdot \boldsymbol{\nabla} + \beta(m + g_\sigma\sigma) + g_\omega\omega^0 + g_\rho\tau_3\rho_3^0 + e\frac{(1-\tau_3)}{2}A^0 \right\} \psi_i = \varepsilon_i \psi_i \quad (6)$$

The effective mass  $m^*(\mathbf{r})$  is defined as

$$m^*(\mathbf{r}) = m + g_\sigma \sigma(\mathbf{r}), \quad (7)$$

and the potential  $V(\mathbf{r})$  as

$$V(\mathbf{r}) = g_\omega \omega^0(\mathbf{r}) + g_\rho \tau_3 \rho_3^0(\mathbf{r}) + e \frac{(1 - \tau_3)}{2} A^0(\mathbf{r}). \quad (8)$$

In nuclei with odd numbers of protons or neutrons time reversal symmetry is broken. The odd particle induces polarization currents and the time-odd components in the meson fields. These fields play an essential role in the description of magnetic moments and of moments of inertia in rotating nuclei. However, their effect on deformations and binding energies is very small and can be neglected to a good approximation.

In order to describe ground-state properties of open-shell nuclei, pairing correlations have to be taken into account. For nuclei close to the  $\beta$ -stability line, pairing has been included in the relativistic mean-field model in the form of a simple BCS approximation [3]. However, for nuclei far from stability the BCS model presents only a poor approximation. In particular, in drip-line nuclei the Fermi level is found close to the particle continuum. The lowest particle-hole or particle-particle modes are often embedded in the continuum, and the coupling between bound and continuum states has to be taken into account explicitly. The BCS model does not provide a correct description of the scattering of nucleonic pairs from bound states to the positive energy continuum [4]; levels high in the continuum become partially occupied. Including the system in a box of finite size leads to unreliable predictions for nuclear radii depending on the size of this box. In the non-relativistic case, a unified description of mean-field and pairing correlations is obtained in the Hartree-Fock-Bogoliubov (HFB) theory [4]. The ground state of a nucleus  $|\Phi\rangle$  is represented as the vacuum with respect to independent quasi-particles. The quasi-particle operators are defined by a unitary Bogoliubov transformation of the single-nucleon creation and annihilation operators. The generalized single-particle Hamiltonian of HFB theory contains two average potentials: the self-consistent field  $\hat{\Gamma}$  which encloses all the long range  $ph$  correlations, and a pairing field  $\hat{\Delta}$  which sums up the  $pp$ -correlations. The expectation value of the nuclear Hamiltonian  $\langle \Phi | \hat{H} | \Phi \rangle$  can be expressed as a function of the hermitian density matrix  $\rho$  and the antisymmetric pairing tensor  $\kappa$ . The variation of the energy functional with respect to  $\rho$  and  $\kappa$  produces the single quasi-particle Hartree-Fock-Bogoliubov equations

$$\begin{pmatrix} \hat{h} - \lambda & \hat{\Delta} \\ -\hat{\Delta}^* & -\hat{h} + \lambda \end{pmatrix} \begin{pmatrix} U_k \\ V_k \end{pmatrix} = E_k \begin{pmatrix} U_k \\ V_k \end{pmatrix}. \quad (9)$$

HFB-theory, being a variational approximation, results in a violation of basic symmetries of the nuclear system. Among the most important is the non conservation of the number of particles. In order that the expectation value of the particle number operator in the ground state equals the number of nucleons, equations (9) contain a chemical potential  $\lambda$  which has to be determined by the particle number subsidiary condition. The column vectors denote the quasi-particle wave functions, and  $E_k$  are the quasi-particle energies.

If the pairing field  $\hat{\Delta}$  is diagonal and constant, HFB reduces to the BCS-approximation. The lower and upper components  $U_k(\mathbf{r})$  and  $V_k(\mathbf{r})$  are proportional, with the BCS-occupation amplitudes  $u_k$  and  $v_k$  as proportionality constants. For a more general pairing interaction this will no longer be the case. As opposed to the functions  $U_k(\mathbf{r})$ , the lower components  $V_k(\mathbf{r})$  are localized functions of  $\mathbf{r}$ , as long as the chemical potential  $\lambda$  is below the continuum limit. Since the densities are bilinear products of  $V_k(\mathbf{r})$  (see Eqs.(15)-(18)), the system is always localized. The HFB wave function can be written either in the quasiparticle basis as a product of independent quasi-particle states, or in the *canonical basis* as a highly correlated BCS-state. In the *canonical basis* nucleons occupy single-particle states. If the chemical potential is close to the continuum, the pairing interaction scatters pairs of nucleons into continuum states. Because of additional pairing correlations, particles which occupy those levels cannot evaporate. Mathematically this is expressed by an additional non-trivial transformation which connects the particle operators in the canonical basis to the quasi-particles of the HFB wave function.

The relativistic extension of the HFB theory was introduced in Ref. [5]. In the Hartree approximation for the self-consistent mean field, the Relativistic Hartree-Bogoliubov (RHB) equations read

$$\begin{pmatrix} \hat{h}_D - m - \lambda & \hat{\Delta} \\ -\hat{\Delta}^* & -\hat{h}_D + m + \lambda \end{pmatrix} \begin{pmatrix} U_k(\mathbf{r}) \\ V_k(\mathbf{r}) \end{pmatrix} = E_k \begin{pmatrix} U_k(\mathbf{r}) \\ V_k(\mathbf{r}) \end{pmatrix}. \quad (10)$$

where  $\hat{h}_D$  is the single-nucleon Dirac Hamiltonian (6), and  $m$  is the nucleon mass. The RHB equations have to be solved self-consistently, with potentials determined in the mean-field approximation from solutions of Klein-Gordon equations

$$[-\Delta + m_\sigma^2] \sigma(\mathbf{r}) = -g_\sigma \rho_s(\mathbf{r}) - g_2 \sigma^2(\mathbf{r}) - g_3 \sigma^3(\mathbf{r}) \quad (11)$$

$$[-\Delta + m_\omega^2] \omega^0(\mathbf{r}) = g_\omega \rho_v(\mathbf{r}) \quad (12)$$

$$[-\Delta + m_\rho^2] \rho^0(\mathbf{r}) = g_\rho \rho_3(\mathbf{r}) \quad (13)$$

$$-\Delta A^0(\mathbf{r}) = e \rho_p(\mathbf{r}). \quad (14)$$

for the sigma meson, omega meson, rho meson and photon field, respectively. Due to charge conservation, only the 3rd-component of the isovector rho meson contributes. The source terms in equations (11) to (14) are sums of bilinear products of baryon amplitudes

$$\rho_s(\mathbf{r}) = \sum_{E_k > 0} V_k^\dagger(\mathbf{r}) \gamma^0 V_k(\mathbf{r}), \quad (15)$$

$$\rho_v(\mathbf{r}) = \sum_{E_k > 0} V_k^\dagger(\mathbf{r}) V_k(\mathbf{r}), \quad (16)$$

$$\rho_3(\mathbf{r}) = \sum_{E_k > 0} V_k^\dagger(\mathbf{r}) \tau_3 V_k(\mathbf{r}), \quad (17)$$

$$\rho_{\text{em}}(\mathbf{r}) = \sum_{E_k > 0} V_k^\dagger(\mathbf{r}) \frac{1 - \tau_3}{2} V_k(\mathbf{r}), \quad (18)$$

where the sums run over all positive energy states. For  $M$  degrees of freedom, for example number of nodes on a radial mesh, the HB equations are  $2M$ -dimensional and have  $2M$  eigenvalues and eigenvectors. To each eigenvector  $(U_k, V_k)$  with eigenvalue  $E_k$ , there corresponds an eigenvector  $(V_k^*, U_k^*)$  with eigenvalue  $-E_k$ . Since baryon quasi-particle operators satisfy fermion commutation relations, it is forbidden to occupy the levels  $E_k$  and  $-E_k$  simultaneously. Usually one chooses the  $M$  positive eigenvalues  $E_k$  for the solution that corresponds to a ground state of a nucleus with even particle number.

The pairing field  $\hat{\Delta}$  in (10) is an integral operator with the kernel

$$\Delta_{ab}(\mathbf{r}, \mathbf{r}') = \frac{1}{2} \sum_{c,d} V_{abcd}(\mathbf{r}, \mathbf{r}') \kappa_{cd}(\mathbf{r}, \mathbf{r}'), \quad (19)$$

where  $a, b, c, d$  denote quantum numbers that specify the Dirac indices of the spinors,  $V_{abcd}(\mathbf{r}, \mathbf{r}')$  are matrix elements of a general two-body pairing interaction, and the pairing tensor is defined

$$\kappa_{cd}(\mathbf{r}, \mathbf{r}') = \sum_{E_k > 0} U_{ck}^*(\mathbf{r}) V_{dk}(\mathbf{r}'). \quad (20)$$

The integral operator  $\hat{\Delta}$  acts on the wave function  $V_k(\mathbf{r})$ :

$$(\hat{\Delta} V_k)(\mathbf{r}) = \sum_b \int d^3 r' \Delta_{ab}(\mathbf{r}, \mathbf{r}') V_{bk}(\mathbf{r}'). \quad (21)$$

The self-consistent solution of the Dirac-Hartree-Bogoliubov integro-differential eigenvalue equations and Klein-Gordon equations for the meson fields determines the nuclear ground state. For systems with spherical symmetry, i.e. single closed-shell nuclei, the coupled system of equations has been solved using finite element methods in coordinate space [6–10], and by expansion in a basis of spherical harmonic oscillator [11–13]. For deformed nuclei the present version of the model does not include solutions in coordinate space. The Dirac-Hartree-Bogoliubov equations and the equations for the meson fields are solved by expanding the nucleon spinors  $U_k(\mathbf{r})$  and  $V_k(\mathbf{r})$ , and the meson fields in terms of the eigenfunctions of a deformed axially symmetric oscillator potential [3]. Of course for nuclei at the drip-lines, solutions in configurational representation might not provide an accurate description of properties that crucially depend on the spatial extension of nucleon densities, as for example nuclear radii.

The eigensolutions of Eq. (10) form a set of orthogonal (normalized) single quasi-particle states. The corresponding eigenvalues are the single quasi-particle energies. The self-consistent iteration procedure is performed in the basis of quasi-particle states. The self-consistent quasi-particle eigenspectrum is then transformed into the canonical basis of single-particle states. The canonical basis is defined to be the one in which the matrix  $R_{kk'} = \langle V_k(\mathbf{r}) | V_{k'}(\mathbf{r}) \rangle$  is diagonal. The transformation to the canonical basis determines the energies and occupation probabilities of single-particle states, which correspond to the self-consistent solution for the ground state of a nucleus.

The details of ground-state properties of nuclei at the drip-lines will depend on the coupling constants and masses of the effective Lagrangian, on the pairing interaction and coupling between bound and continuum states. Several parameter sets of the mean-field Lagrangian have been derived that provide a satisfactory description of nuclear properties along the  $\beta$ -stability line. In particular, NL1 [14], NL-SH [15], and NL3 [16]. The effective forces NL1 and NL-SH have been frequently used to calculate properties of nuclear matter and of finite nuclei, and have become standard parameterizations for relativistic mean-field calculations. The parameter set NL3 has been derived more recently [16], by adjusting to ground state properties of a large number of spherical nuclei. Properties calculated with NL3 indicate that this is probably the best RMF effective interaction so far, both for nuclei at and away from the line of  $\beta$ -stability.

In many applications of the relativistic mean-field model pairing correlations have been taken into account in a very phenomenological way in the BCS-theory with monopole pairing force adjusted to the experimental odd-even mass differences. This framework obviously cannot be applied to the description of the coupling to the particle continuum in nuclei close to the drip-line. The question therefore arises, which pairing interaction  $V_{abcd}(\mathbf{r}, \mathbf{r}')$  should be used in Eq. (19). In principle, in Ref. [5] a fully relativistic derivation of the pairing force has been developed, starting from the Lagrangian (1). Using the Gorkov factorization technique, it has been possible to demonstrate that the pairing interaction results from the one-meson exchange ( $\sigma$ -,  $\omega$ - and  $\rho$ -mesons). In practice, however, it turns out that the pairing correlations calculated in this way, with coupling constants taken from standard parameter sets of the RMF model, are much too strong. The repulsion produced by the exchange of vector mesons at short distances results in a pairing gap at the Fermi surface that is by a factor three too large. However, as has been argued in many applications of the Hartree-Fock-Bogoliubov theory, there is no real reason to use the same effective forces in both the particle-hole and particle-particle channel. In a first-order approximation, the effective interaction contained in the mean-field  $\hat{\Gamma}$  is a  $G$ -matrix, the sum over all ladder diagrams. The effective force in the  $pp$  channel, i.e. in the pairing potential  $\hat{\Delta}$ , should be the  $K$  matrix, the sum of all diagrams irreducible in  $pp$ -direction. Since very little is known about this matrix in the relativistic approach, in most applications of the RHB model a phenomenological pairing interaction has been used, the pairing part of the Gogny force [17],

$$V^{pp}(1, 2) = \sum_{i=1, 2} e^{-((\mathbf{r}_1 - \mathbf{r}_2)/\mu_i)^2} (W_i + B_i P^\sigma - H_i P^\tau - M_i P^\sigma P^\tau), \quad (22)$$

with the set D1S [17] for the parameters  $\mu_i$ ,  $W_i$ ,  $B_i$ ,  $H_i$  and  $M_i$  ( $i = 1, 2$ ). This force has been very carefully adjusted to the pairing properties of finite nuclei all over the periodic table. In particular, the basic advantage of the Gogny force is the finite range, which automatically guarantees a proper cut-off in momentum space. The fact that it is a non-relativistic interaction has little influence on the results of RHB calculations. A relativistic pairing force should include both a Lorentz-scalar and a Lorentz-vector part, as for example the interactions derived in Refs. [5]. However, as opposed to the mean-field  $\hat{\Gamma}$ , where the contribution of the small components in the Dirac spinors is reflected in a very large spin-orbit splitting and where the difference between the scalar density (15) and the vector density (16) leads to saturation, the contribution of these components in the pairing channel can be neglected to a very good approximation. In the pairing channel only levels in the vicinity of the Fermi surface are really important, or in other words, pairing is a completely non-relativistic effect.

In order to test the combination of the NL3 effective interaction for the mean-field Lagrangian, and the Gogny interaction with the parameter D1S in the pairing channel, ground-state properties of a chain of Ni and Sn isotopes have been calculated in Ref. [12]. The analysis has shown that the NL3 effective force provides an accurate description of systems with very different number of neutrons. The correct isospin dependence of NL3 implies that this interaction can be used to make reliable predictions about drip-line nuclei. In Fig. 1 the one- and two-neutron separation energies are shown for the Sn ( $50 \leq N \leq 88$ ) isotopes. The values that correspond to the self-consistent RHB ground-states are compared with experimental data and extrapolated values from Ref. [18]. The theoretical values reproduce in detail the experimental separation energies. The model describes not only the empirical values within one major neutron shell, but it also reproduces the transitions between major shells. The agreement with experimental data is also very good for the Ni isotopes. For the total binding energies, except for the region around  $^{60}\text{Ni}$  and for  $^{100-102}\text{Sn}$ , the absolute differences between the calculated and experimental masses are less than 2 MeV. For Ni the model predicts weaker binding for  $N \leq 40$ . Compared to experimental values, the theoretical binding energies are  $\approx 1$  MeV larger for neutrons in the  $1g_{9/2}$  orbital ( $40 \leq N \leq 50$ ). For Sn isotopes the results of model calculation in general display stronger binding. The differences are somewhat larger for  $^{100-102}\text{Sn}$ , but for these nuclei it is expected that the masses might be strongly affected by proton-neutron residual short-range correlations. Excellent results have also been obtained in the comparison between calculated and experimental neutron and proton rms radii for the Ni and Sn isotopes.

In Ref. [19] it has been shown that constrained RMF calculations with the NL3 effective force reproduce the excitation energies of superdeformed minima relative to the ground-state in  $^{194}\text{Hg}$  and  $^{194}\text{Pb}$ . In the same work the NL3 interaction was also used for calculations of binding energies and deformation parameters of rare-earth nuclei.

All theoretical analyses have shown that the combination NL3 + D1S could be expected to predict relevant results also in the regions of drip-line nuclei. In all the applications of the RHB model which are described in the present review, the NL3 effective force has been used in the mean-field Lagrangian, and the Gogny D1S interaction in the pairing channel.

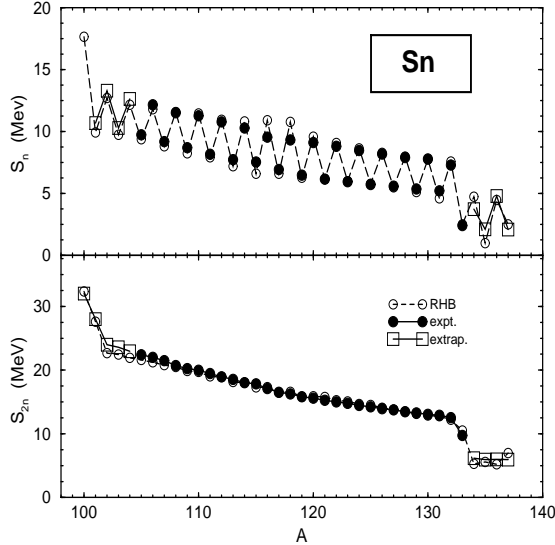


**FIGURE 1.** One and two-neutron separation energies for Sn isotopes calculated in the RHB model and compared with experimental (filled circles) and extrapolated (squares) data from the compilation of G. Audi and A. H. Wapstra.

The spin-orbit interaction plays a central role in nuclear structure. It is rooted in the basis of the nuclear shell model, where its inclusion is essential in order to reproduce the experimentally established magic numbers. In non-relativistic models based on the mean-field approximation, the spin-orbit potential is included in a phenomenological way. Of course such an ansatz introduces an additional parameter: the strength of the spin-orbit interaction. The value of this parameter is usually adjusted to the experimental spin-orbit splittings in spherical nuclei, for example  $^{16}\text{O}$ . On the other hand, in the relativistic framework the nucleons are described as Dirac spinors. This means that in the relativistic description of the nuclear many-body problem, the spin-orbit interaction arises naturally from the Dirac-Lorenz structure of the effective Lagrangian. No additional strength parameter is necessary, and relativistic models reproduce the empirical spin-orbit splittings. It is then of special interest to study the predictions of the relativistic model for the isovector properties of the spin-orbit term of the effective interaction [9]. In the first order approximation, and assuming spherical symmetry, the spin-orbit term can be written as

$$V_{s.o.} = \frac{1}{r} \frac{\partial}{\partial r} V_{ls}(r), \quad (23)$$

where  $V_{ls}$  is the spin-orbit potential [2].

$$V_{ls} = \frac{m}{m_{eff}}(V - S). \quad (24)$$

$V$  and  $S$  denote the repulsive vector and the attractive scalar potentials, respectively.  $m_{eff}$  is the effective mass

$$m_{eff} = m - \frac{1}{2}(V - S). \quad (25)$$

Using the vector and scalar potentials from the self-consistent ground-state solutions, from (23) - (25) the corresponding spin-orbit terms have been computed for the Ni isotopes. They are displayed in Fig. 2 as function of

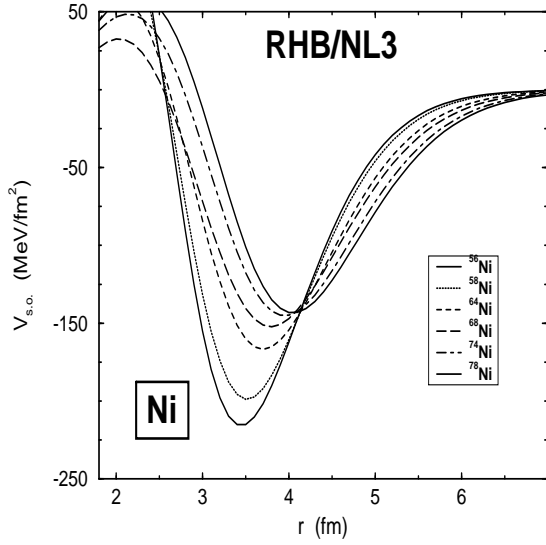


**FIGURE 2.** Radial dependence of the spin-orbit term of the potential in self-consistent solutions for the ground-states of Ni ( $28 \leq N \leq 50$ ) nuclei.

the radial distance from the center of the nucleus. The magnitude of the spin-orbit term  $V_{s.o.}$  decreases with the number of neutrons. If  $^{56}\text{Ni}$  with  $^{78}\text{Ni}$  are compared, the reduction is  $\approx 35\%$  in the surface region. This implies a significant weakening of the spin-orbit interaction. The minimum of  $V_{s.o.}$  is also shifted outwards, and this reflects the larger spatial extension of the scalar and vector densities, which become very diffuse on the surface. The effect is stronger in light nuclei [9], while it has been shown in Ref. [12] that the reduction of the spin-orbit term seems to be less pronounced in the Sn isotopes. These results indicate that the weakening of the spin-orbit interaction might not be that important in heavy nuclei. The effect is reflected in the calculated energy splittings between spin-orbit partners. The gradual decrease of the energy gap between single-particle levels is consistent with the weakening of the spin-orbit term of the effective interaction.

## NEUTRON HALO IN LIGHT NUCLEI

In some loosely bound systems at the drip-lines, the neutron density distribution displays an extremely long tail: the neutron halo. The resulting large interaction cross sections have provided the first experimental evidence for halo nuclei [20]. The neutron halo phenomenon has been studied with a variety of theoretical models [21,22]. For very light nuclei in particular, models based on the separation into core plus valence space nucleons (three-body Borromean systems) have been employed. In heavier neutron-rich nuclei one expects that mean-field models should provide a better description of ground-state properties. In a mean-field description, the neutron halo and the stability against nucleon emission can only be explained with the inclusion of pairing correlations. Both the properties of single-particle states near the neutron Fermi level, and the pairing interaction, are important in the formation of the neutron halo.

The details of the formation of the neutron halo in Ne isotopes have been studied in Ref. [7]. In Fig. 3a the rms radii for Ne isotopes are plotted as functions of neutron number. Neutron and proton rms radii are shown, and the  $N^{1/3}$  curve normalized so that it coincides with the neutron radius in  $^{20}\text{Ne}$ . The neutron radii follow the mean-field  $N^{1/3}$  curve up to  $N \approx 22$ . For larger values of  $N$  the neutron radii display a sharp increase, while the proton radii stay practically constant. This sudden increase in neutron rms radii has been interpreted as evidence for the formation of a multi-particle halo. The phenomenon is also observed in the plot of proton and neutron density distributions 4. The proton density profiles do not change with the number of neutrons, while the neutron density distributions display an abrupt change between  $^{30}\text{Ne}$  and  $^{32}\text{Ne}$ . The microscopic origin of the neutron halo has been found in a delicate balance of the self-consistent mean-field and the pairing field. This is shown in Fig. 3b, where the neutron single-particle states  $1f_{7/2}$ ,  $2p_{3/2}$  and  $2p_{1/2}$  in the canonical basis, and the Fermi energy are plotted as function of the neutron number. For  $N \leq 22$  the triplet of states is high in the continuum, and the Fermi level uniformly increases toward zero. The triplet approaches zero energy, and a gap is formed between these states and all other states in the continuum. The shell structure dramatically changes at  $N \geq 22$ . Between  $N = 22$  and  $N = 32$  the Fermi level is practically constant and very close to the continuum. The addition of neutrons in this region of the drip does not increase the binding. Only the spatial extension of neutron distribution displays an increase. The formation of the neutron halo is related to the quasi-degeneracy of the triplet of states  $1f_{7/2}$ ,  $2p_{3/2}$  and  $2p_{1/2}$ . The pairing interaction promotes neutrons from the  $1f_{7/2}$  orbital to the  $2p$  levels. Since these levels are so close in energy, the total binding energy does not change significantly. Due to their small centrifugal barrier, the  $2p_{3/2}$  and  $2p_{1/2}$  orbitals form the halo. A similar mechanism has been suggested in Ref. [23] for the experimentally observed halo in the nucleus  $^{11}\text{Li}$ . There the formation of the halo is determined by the pair of neutron levels  $1p_{1/2}$  and  $2s_{1/2}$ . A giant halo has been also predicted for Zirconium isotopes [24]. In that case the halo originates from the neutron orbitals  $2f_{7/2}$ ,  $3p_{3/2}$  and  $3p_{1/2}$ .

RHB calculations reported in Ref. [8] have shown that the triplet of single-particle states near the neutron Fermi level:  $1f_{7/2}$ ,  $2p_{3/2}$  and  $2p_{1/2}$ , and the neutron pairing interaction determine the location of the neutron drip-line, the formation of the neutron skin, or eventually of the neutron halo in light nuclei. For C, N, O and F the triplet is still high in the continuum at  $N = 20$ , and the pairing interaction is too weak to promote pairs of neutrons into these levels. All mean-field effective interactions predict similar results, and the neutron drip is found at  $N = 18$  or  $N = 20$ . For Ne, Na, and Mg the states  $1f_{7/2}$ ,  $2p_{3/2}$  and  $2p_{1/2}$  are much lower in energy, and for  $N \geq 20$  the neutrons populate these levels. The neutron drip can change by as much as twelve neutrons. The model predicts the formation of neutron skin, and eventually neutron halo in Ne and Na. This is due to the fact that the triplet of states is almost degenerate in energy for  $N \geq 20$ . For Mg the  $1f_{7/2}$  lies deeper and neutrons above the  $s-d$  shell will exclusively populate this level, resulting in a deformation of the mean field. When the neutron single-particle levels are displayed as function of the number of protons, it turns out that the binding of neutrons is determined by the  $1f_{7/2}$  orbital which is found to be parallel to the slope of the Fermi level. The reduction of the spin-orbit splitting  $1f_{7/2} - 1f_{5/2}$  close to the neutron drip-line has been related to the isospin dependence of the spin-orbit interaction. Density distributions have been analyzed, and the resulting surface thickness and diffuseness parameter reflect the

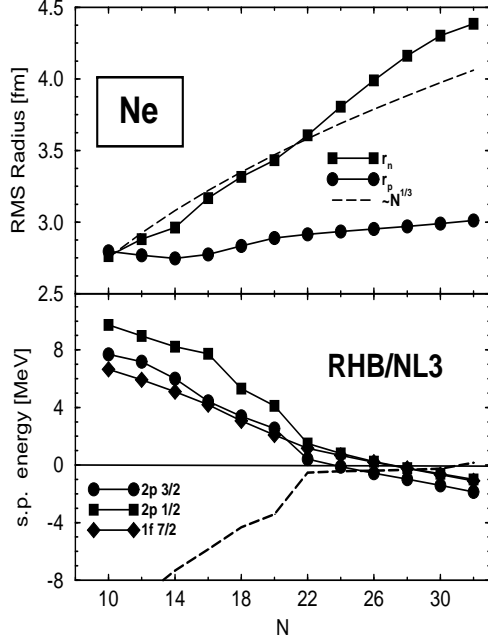


**FIGURE 3.** Calculated proton and neutron *rms* radii for Ne isotopes (top), and the 1f-2p single-particle neutron levels in the canonical basis (bottom).

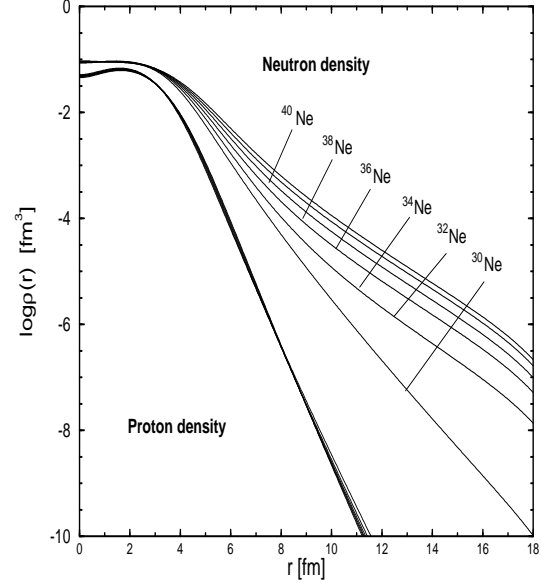


**FIGURE 4.** Proton and neutron density distribution for Ne isotopes.

reduction of the spin-orbit term of the effective potential in the surface region of neutron-rich nuclei.

In Ref. [10] an interesting study of  $\Lambda$ -hypernuclei with a large neutron excess has been reported. In particular, the effects of the  $\Lambda$  hyperon on Ne isotopes with neutron halo have been studied. Although the inclusion of the  $\Lambda$  does not produce excessive changes in bulk properties of these nuclei, it can shift the neutron drip by stabilizing an otherwise unbound core nucleus at the drip-line. The microscopic mechanism through which additional neutrons are bound to the core originates from the increase in magnitude of the spin-orbit term in presence of the  $\Lambda$  particle. The  $\Lambda$  in its ground state produces only a fractional change in the central mean-field potential. On the other hand, through a purely relativistic effect, it notably changes the spin-orbit term in the surface region, providing additional binding for the outermost neutrons. The effect can be illustrated on the example of  $^{30}\text{Ne}$  and the corresponding hypernucleus  $^{31}\Lambda\text{Ne}$ . The mean field potential, in which the nucleons move, results from the cancelation of two large meson potentials: the attractive scalar potential S and the repulsive vector potential V:  $V+S$ . The spin-orbit potential, on the other hand, arises from the very strong anti-nucleon potential  $V-S$ . Therefore, while in the presence of the  $\Lambda$  the changes in V and S cancel out in the mean-field potential, they are amplified in  $V_{ls}$ . For the core  $^{30}\text{Ne}$  the values of the scalar (S) and vector (V) potential in the center of the nucleus are -380 MeV and 308 MeV, respectively. For  $^{31}\Lambda\text{Ne}$  the corresponding values are: -412 MeV and 336 MeV. The addition of the  $\Lambda$  particle changes the value of the mean-field potential in the center of the nucleus by 4 MeV, but it changes the anti-nucleon potential by 60 MeV. This is reflected in the corresponding spin-orbit term of the effective potential, which provides more binding for states close to the Fermi surface. The additional binding stabilizes the hypernuclear core.

## SHAPE COEXISTENCE IN THE DEFORMED N = 28 REGION

The region of neutron-rich  $N \approx 28$  nuclei displays many interesting phenomena: the average nucleonic potential is modified, shell effects are suppressed, large quadrupole deformations are observed as well as shape coexistence, isovector quadrupole deformations are predicted at drip-lines. The detailed knowledge of the microscopic structure of these nuclei is also essential for a correct description of the nucleosynthesis of the heavy Ca, Ti and Cr isotopes. In the RHB model the structure of exotic neutron rich-nuclei with  $12 \leq Z \leq 20$  has been studied, and in particular the light  $N = 28$  nuclei. Especially interesting is the influence of the spherical shell  $N = 28$  on the structure of nuclei below  $^{48}\text{Ca}$ , the deformation effects that result from the  $1f7/2 \rightarrow fp$  core breaking, and the shape coexistence

phenomena predicted for these  $\gamma$ -soft nuclei.

The results of Skyrme Hartree-Fock + BCS and RMF + BCS calculations of Ref. [25] have shown that neutron-rich Si, S and Ar isotopes can be considered as  $\gamma$ -soft, with deformations depending on subtle interplay between the deformed gaps  $Z = 16$  and  $18$ , and the spherical gap at  $N = 28$ . Because of cross-shell excitations to the  $2p_{3/2}$ ,  $2p_{1/2}$  and  $1f_{5/2}$  shells, the  $N = 28$  gap appears to be broken in most cases. In the RMF + BCS analysis of Ref. [26], a careful study of the phenomenon of shape coexistence was performed for nuclei in this region. It was shown that several Si and S isotopes exhibit shape coexistence: two minima with different deformations occur in the binding energy. The energy difference between the two minima is of the order of few hundred keV. For  $^{44}\text{S}$  the calculated difference was only 30 keV. The results obtained with the two models, HF and RMF, were found to be similar, although also important differences were calculated, as for example, the equilibrium shape of the  $N = 28$  nucleus  $^{44}\text{S}$ . The comparison with results of FRDM and ETFSI calculations, has also shown the importance of a unified and self-consistent description of mean-field and pairing correlations in this region of transitional nuclei.

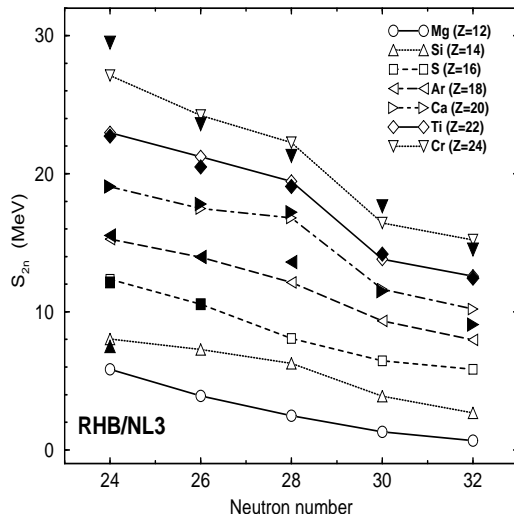


**FIGURE 5.** Two-neutron separation energies in the  $N \approx 28$  region calculated in the RHB model and compared with experimental data (filled symbols) from the compilation of G. Audi and A. H. Wapstra.

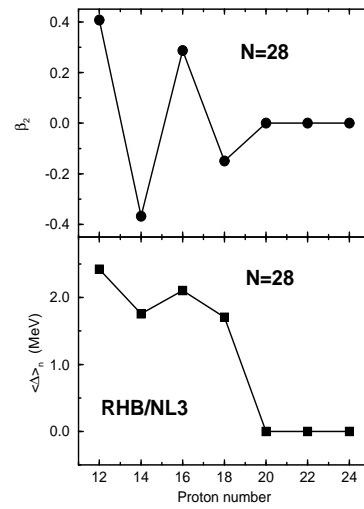


**FIGURE 6.** Self-consistent RHB quadrupole deformations for ground-states of the  $N = 28$  isotones (top). Average neutron pairing gaps  $\langle \Delta_N \rangle$  as function of proton number (bottom).

In Fig. 5 the two-neutron separation energies are plotted for the even-even nuclei  $12 \leq Z \leq 24$  and  $24 \leq Z \leq 32$ . The values that correspond to the self-consistent RHB ground-states (symbols connected by lines) are compared with experimental data and extrapolated values from Ref. [18] (filled symbols). Except for Mg and Si, these isotopes are not at the drip-lines. The theoretical values reproduce in detail the experimental separation energies, except for  $^{48}\text{Cr}$ . In general, it has been found that RHB model binding energies are in very good agreement with experimental data when one of the shells (proton or neutron) is closed, or when valence protons and neutrons occupy different major shells (i.e. below and above  $N$  and/or  $Z = 20$ ). The differences are more pronounced when both protons and neutrons occupy the same major shell, and especially for the  $N = Z$  nuclei. For these nuclei additional correlations should be taken into account, and in particular proton-neutron pairing could have a strong influence on the masses.

The predicted mass quadrupole deformations for the ground states of  $N = 28$  nuclei are shown in the upper panel of Fig. 6. The staggering between prolate and oblate configurations indicates that the potential is  $\gamma$ -soft. The absolute values of the deformation decrease towards the  $Z = 20$  closed shell. Starting with Ca, the  $N = 28$  nuclei are spherical in the ground state. The calculated quadrupole deformations are in agreement with previously reported theoretical results [25] (prolate for  $Z = 16$ , oblate for  $Z = 18$ ), and with available experimental data:  $|\beta_2| = 0.258(36)$  for  $^{44}\text{S}$  [27,28], and  $|\beta_2| = 0.176(17)$  for  $^{46}\text{Ar}$  [29]. Experimental data (energies of  $2_1^+$  states and  $B(E2; 0_{g.s.}^+ \rightarrow 2_1^+)$  values) do not determine the sign of deformation, i.e. do not differentiate between prolate and oblate shapes. In the lower panel of Fig. 6 the average values of the neutron pairing gaps for occupied canonical states are displayed.  $\langle \Delta_N \rangle$  provides an excellent quantitative measure of pairing correlations. The calculated

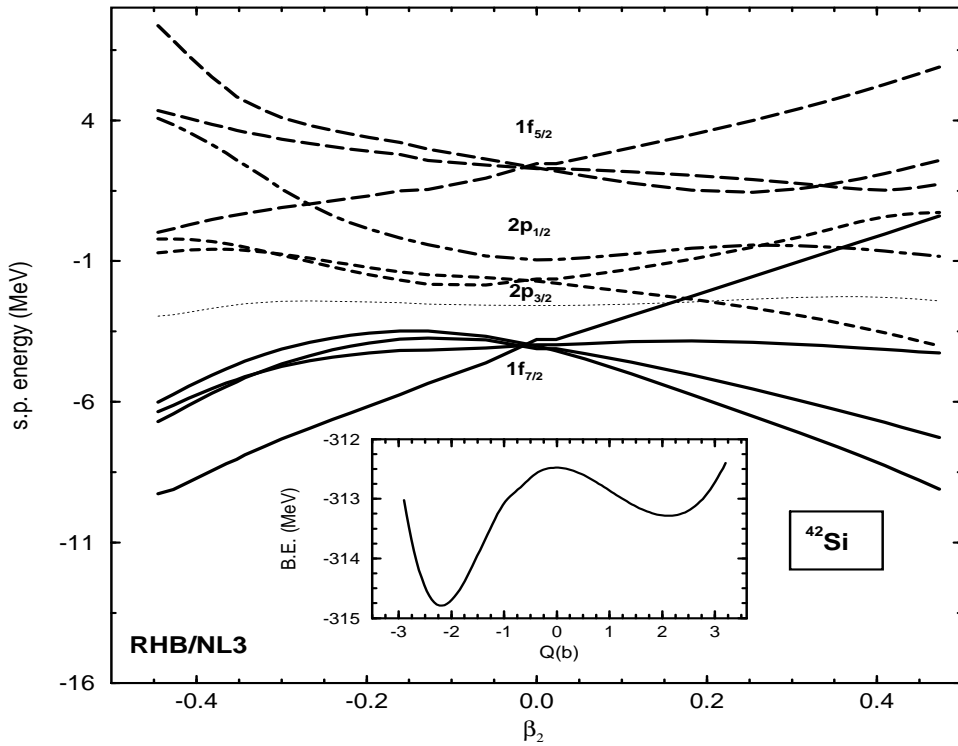


**FIGURE 7.** The neutron single-particle levels for  $^{42}\text{Si}$  as function of the quadrupole deformation. The energies in the canonical basis correspond to ground-state RHB solutions with constrained quadrupole deformation. The dotted line denotes the neutron Fermi level. In the insert the corresponding total binding energy curve is shown.

values of  $\langle \Delta_N \rangle \approx 2$  MeV correspond to those found in open-shell Ni and Sn isotopes [12]. The spherical shell closure  $N = 28$  is strongly suppressed for nuclei with  $Z \leq 18$ , and only for  $Z \geq 20$  neutron pairing correlations vanish.

In the fully microscopic and self-consistent RHB model, the details of the single-neutron levels can be analyzed, and the formation of minima in the binding energy can be studied. Figs. 7-9 display the single-neutron levels in the canonical basis for the  $N = 28$  nuclei  $^{42}\text{Si}$ ,  $^{44}\text{S}$ , and  $^{46}\text{Ar}$ , respectively. The single-neutron eigenstates of the density matrix result from constrained RHB calculations performed by imposing a quadratic constraint on the quadrupole moment. The canonical states are plotted as function of the quadrupole deformation, and the dotted curve denotes the position of the Fermi level. In the insert the corresponding total binding energy curve as function of the quadrupole moment is shown. For  $^{42}\text{Si}$  the binding energy displays a deep oblate minimum ( $\beta_2 \approx -0.4$ ). The second, prolate minimum is found at an excitation energy of  $\approx 1.5$  MeV. Shape coexistence is more pronounced for  $^{44}\text{S}$ . The ground state is prolate deformed, the calculated deformation in excellent agreement with experimental data [27,28]. The oblate minimum is found only  $\approx 200$  keV above the ground state. Finally, for the nucleus  $^{46}\text{Ar}$  a very flat energy surface is found on the oblate side. The deformation of the ground-state oblate minimum agrees with experimental data [29], the spherical state is only few keV higher. It is also interesting to observe how the spherical gap between the  $1f_{7/2}$  orbital and the  $2p_{3/2}$ ,  $2p_{1/2}$  orbitals varies with proton number. While the gap is really strongly reduced for  $^{42}\text{Si}$  and  $^{44}\text{S}$ , in the  $Z = 18$  isotope  $^{46}\text{Ar}$  the spherical gap is  $\approx 4$  MeV. Of course from  $^{48}\text{Ca}$  the  $N = 28$  nuclei become spherical. Therefore the single-neutron canonical states in Figs. 7-9 clearly display the disappearance of the spherical  $N = 28$  shell closure for neutron-rich nuclei below  $Z = 18$ .

## NUCLEI AT THE PROTON DRIP-LINES

The decay by direct proton emission provides the opportunity to study the structure of systems beyond the drip-line. The phenomenon of ground-state proton radioactivity is determined by a delicate interplay between the Coulomb and centrifugal terms of the effective potential. While low- $Z$  nuclei lying beyond the proton drip-line exist only as short lived resonances, the relatively high potential energy barrier enables the observation of ground-state

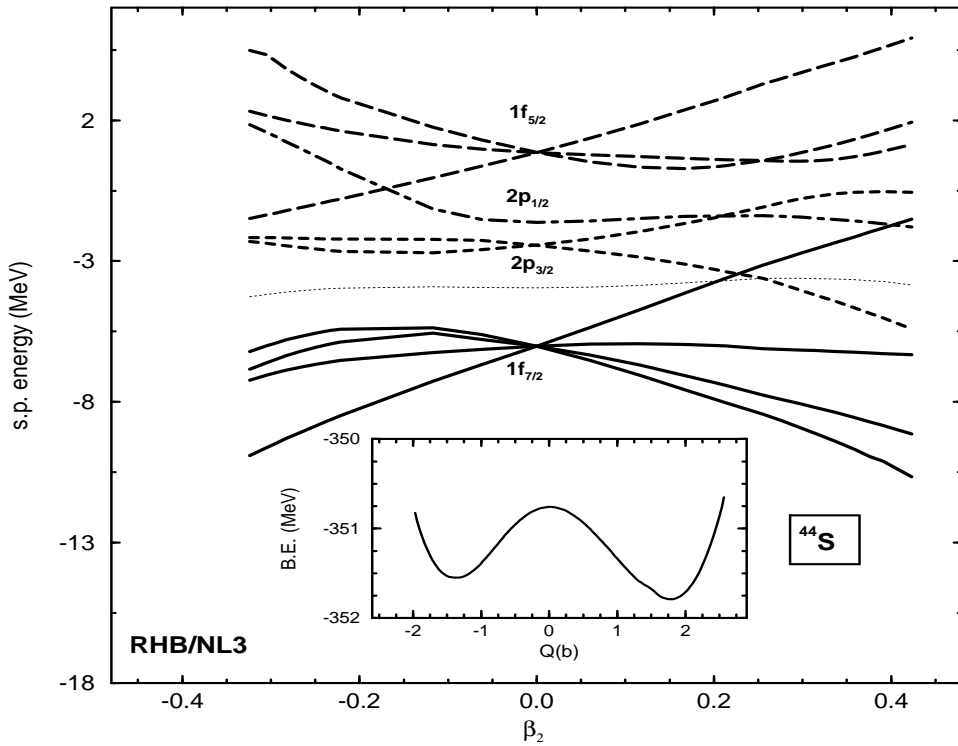


**FIGURE 8.** The same as in Fig. 7, but for  $^{44}\text{S}$ .

proton emission from medium-heavy and heavy nuclei. At the drip-lines proton emission competes with  $\beta^+$  decay; for heavy nuclei also fission or  $\alpha$  decay can be favored. The proton drip-line has been fully mapped up to  $Z = 21$ , and possibly for odd- $Z$  nuclei up to In [30]. No examples of ground-state proton emission have been discovered below  $Z = 50$ .

The RHB model with finite range-pairing has been applied in the study of ground-state properties of spherical even-even nuclei  $14 \leq Z \leq 28$  and  $N = 18, 20, 22$  [13]. While for these neutron numbers the nuclei with  $14 \leq Z \leq 20$  are not really very proton-rich, nevertheless they are useful for a comparison of the model calculations with experimental data. Of particular interest are the predictions of the model for the proton-rich nuclei in the  $1\text{f}_{7/2}$  region. These nuclei have recently been extensively investigated in experiments involving fragmentation of  $^{58}\text{Ni}$ . The principal motivation of many experimental studies in this region is the possible occurrence of the two-proton ground-state radioactivity. In particular, the region around  $^{48}\text{Ni}$  is expected to contain nuclei which are two-proton emitters. On the other hand, because of the Coulomb barrier at the proton drip-line, the emission of a pair of protons may be strongly delayed for nuclei with small negative two-proton separation energies.

The two-proton separation energies that correspond to the self-consistent RHB ground-states for the even-even nuclei  $14 \leq Z \leq 28$  and  $N = 18, 20, 22$ , have been compared with experimental data and extrapolated values from Ref. [18]. The theoretical values reproduce in detail the experimental separation energies, except for  $^{38}\text{Ca}$  and  $^{44}\text{Ti}$ . In Table 1 the calculated total binding energies for the  $N = 18, 20, 22$  isotones are displayed in comparison with empirical values. As has been already shown in the previous section for the neutron rich  $N = 28$  nuclei, the RHB model results are in very good agreement with experimental data when one of the shells (proton or neutron) is closed, or when valence protons and neutrons occupy different major shells (i.e. below and above  $N$  and/or  $Z = 20$ ). The absolute differences between the calculated and experimental masses are less than 2 MeV. The differences are larger when both proton and neutron valence particles (holes) occupy the same major shell, and especially for the  $N = Z$  nuclei  $^{36}\text{Ar}$  and  $^{44}\text{Ti}$ .

The RHB results should be also compared with recently reported self-consistent mean-field calculations of Ref. [31], and with properties of proton-rich nuclei calculated with the shell model [32]. The calculations of Ref. [31] have been performed for several mean-field models (Hartree-Fock, Hartree-Fock-Bogoliubov, and relativistic mean-field), and for a number of effective interactions. The results systematically predict the two-proton drip-line to lie between  $^{42}\text{Cr}$  and  $^{44}\text{Cr}$ ,  $^{44}\text{Fe}$  and  $^{46}\text{Fe}$ , and  $^{48}\text{Ni}$  and  $^{50}\text{Ni}$ . Recent studies of proton drip-line nuclei in this region have been performed in experiments based on  $^{58}\text{Ni}$  fragmentation on a beryllium target, and evidence has been reported for

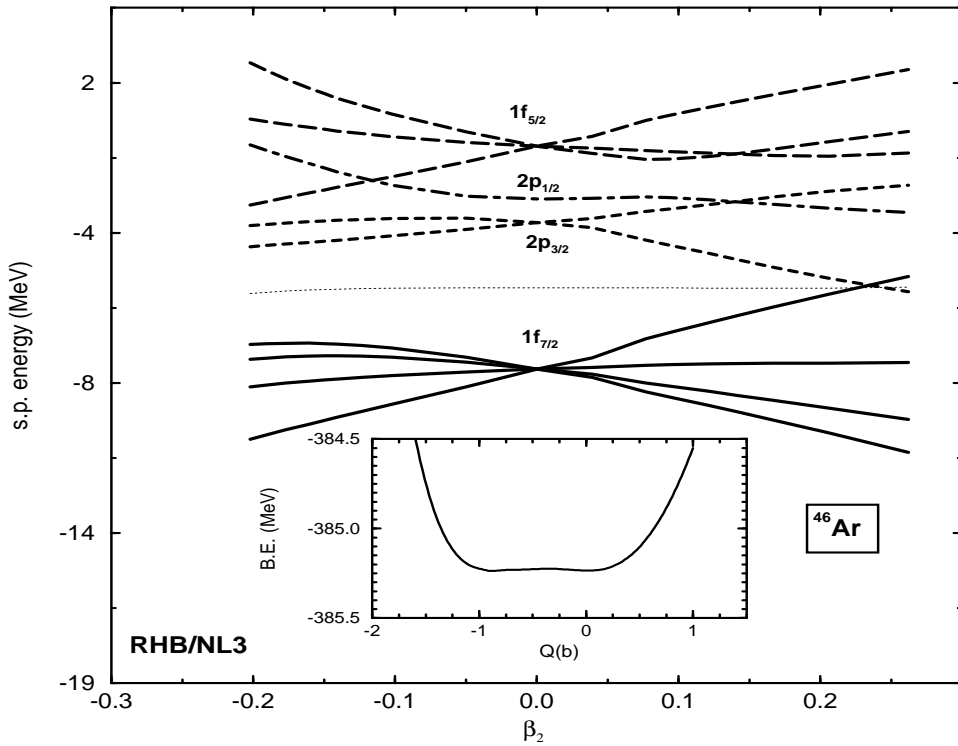


**FIGURE 9.** The same as in Fig. 7, but for  $^{46}\text{Ar}$ .

particle stability of  $^{50}\text{Ni}$  [33]. In the shell-model calculations of Ref. [32] absolute binding energies were evaluated by computing the Coulomb energy shifts between mirror nuclei, and adding this shift to the experimentally determined binding energy of the neutron rich isotope. The calculated two-proton separation energies predicted a proton drip-line in agreement with experimental data and with the mean-field results [31]. Compared to the RHB results, the shell-model total binding energies are in somewhat better agreement with experimental data. However, the two models give almost identical values for the extracted two-proton separation energies of the drip-line nuclei. The self-consistent RHB NL3+D1S two-proton separation energies at the drip-line are also very close to the values that result from non-relativistic HFB+Gogny (D1S) calculation of Ref. [31].

Proton radioactivity in odd-Z nuclei has been investigated in the two spherical regions from  $51 \leq Z \leq 55$  and  $69 \leq Z \leq 83$ . The systematics of proton decay spectroscopic factors is consistent with half-lives calculated in the spherical WKB or DWBA approximations. Recently reported proton decay rates [34] indicate that the missing region of light rare-earth nuclei contains strongly deformed nuclei at the drip-lines. The lifetimes of deformed proton emitters provide direct information on the last occupied Nilsson configuration, and therefore on the shape of the nucleus. Modern models for proton decay rates from deformed nuclei have only recently been developed. However,

**TABLE 1.** Comparison between calculated and empirical binding energies.  
All values are in units of MeV; empirical values are displayed in parentheses.

$^{32}\text{Si}$	269.02 (271.41)	$^{40}\text{Ar}$	343.97 (343.81)	$^{44}\text{Cr}$	351.65 (349.99)
$^{34}\text{Si}$	284.42 (283.43)	$^{38}\text{Ca}$	313.11 (313.04)	$^{46}\text{Cr}$	380.19 (381.98)
$^{36}\text{Si}$	293.08 (292.02)	$^{40}\text{Ca}$	341.99 (342.05)	$^{44}\text{Fe}$	312.07 (-)
$^{34}\text{S}$	288.10 (291.84)	$^{42}\text{Ca}$	362.95 (361.90)	$^{46}\text{Fe}$	352.25 (350.20)
$^{36}\text{S}$	307.98 (308.71)	$^{40}\text{Ti}$	315.39 (314.49)	$^{48}\text{Fe}$	384.42 (385.19)
$^{38}\text{S}$	320.77 (321.05)	$^{42}\text{Ti}$	348.35 (346.91)	$^{46}\text{Ni}$	306.72 (-)
$^{36}\text{Ar}$	302.52 (306.71)	$^{44}\text{Ti}$	373.15 (375.47)	$^{48}\text{Ni}$	349.92 (-)
$^{38}\text{Ar}$	327.34 (327.06)	$^{42}\text{Cr}$	314.94 (314.20)	$^{50}\text{Ni}$	385.52 (385.50)

even the most realistic calculations are not based on a fully microscopic and self-consistent description of proton unstable nuclei. In particular, such a description should also include important pairing correlations.

Fig. 10 displays the one-proton separation energies for the odd-Z nuclei  $59 \leq Z \leq 69$ , as function of the number of neutrons. The model predicts the drip-line nuclei:  $^{124}\text{Pr}$ ,  $^{129}\text{Pm}$ ,  $^{134}\text{Eu}$ ,  $^{139}\text{Tb}$ ,  $^{146}\text{Ho}$ , and  $^{152}\text{Tm}$ . In heavy proton drip-line nuclei the potential energy barrier, which results from the superposition of the Coulomb and centrifugal potentials, is relatively high. For the proton decay to occur the odd valence proton must penetrate the potential barrier, and this process competes with  $\beta^+$  decay. Since the half-life for proton decay is inversely proportional to the energy of the odd proton, in many nuclei the decay will not be observed immediately after the drip-line. Proton radioactivity is expected to dominate over  $\beta^+$  decay only when the energy of the odd proton becomes relatively high. This is also a crucial point for the relativistic description of proton emitters, since the precise values of the separation energies depend on the isovector properties of the spin-orbit interaction.

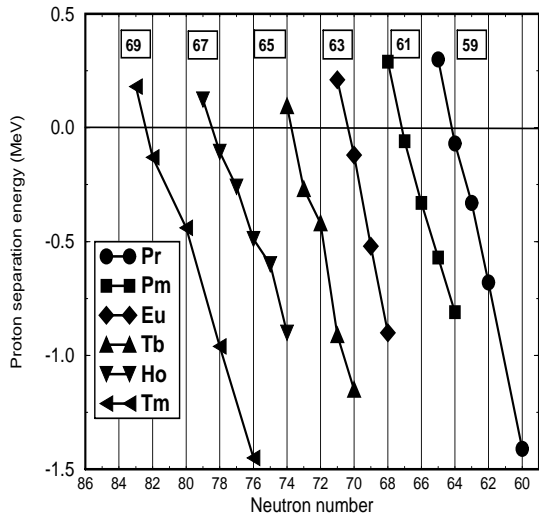


**FIGURE 10.** Calculated one-proton separation energies for odd-Z nuclei  $59 \leq Z \leq 69$  at and beyond the drip-line.

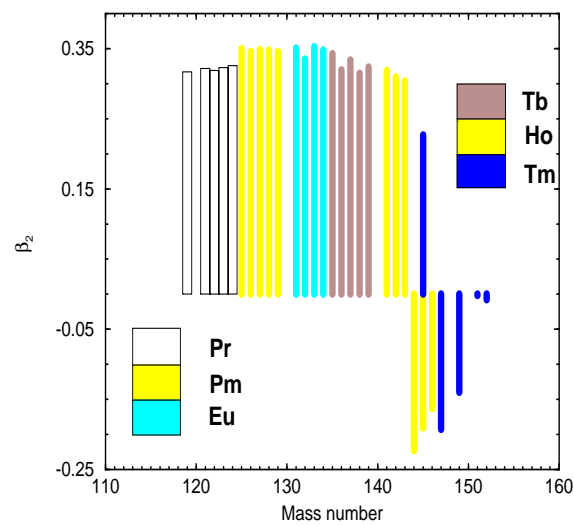


**FIGURE 11.** Self-consistent ground-state quadrupole deformations for the odd-Z nuclei  $59 \leq Z \leq 69$  at the proton drip-line.

The calculated separation energies should be compared with recently reported experimental data on proton radioactivity from  $^{131}\text{Eu}$ ,  $^{141}\text{Ho}$  [34],  $^{145}\text{Tm}$  [35], and  $^{147}\text{Tm}$  [36]. The  $^{131}\text{Eu}$  transition has an energy  $E_p = 0.950(8)$  MeV and a half-life  $26(6)$  ms, consistent with decay from either  $3/2^+[411]$  or  $5/2^+[413]$  Nilsson orbital. For  $^{141}\text{Ho}$  the transition energy is  $E_p = 1.169(8)$  MeV, and the half-life  $4.2(4)$  ms is assigned to the decay of the  $7/2^-[523]$  orbital. The calculated proton separation energy, both for  $^{131}\text{Eu}$  and  $^{141}\text{Ho}$ , is of  $-0.9$  MeV. In the RHB calculation for  $^{131}\text{Eu}$  the odd proton occupies the  $5/2^+[413]$  orbital, while the ground state of  $^{141}\text{Ho}$  corresponds to the  $7/2^-[523]$  proton orbital. This orbital is also occupied by the odd proton in the calculated ground states of  $^{145}\text{Tm}$  and  $^{147}\text{Tm}$ . The calculated proton separation energies:  $-1.46$  MeV in  $^{145}\text{Tm}$ , and  $-0.96$  MeV in  $^{147}\text{Tm}$ , are compared with the experimental values for transition energies:  $E_p = 1.728(10)$  MeV in  $^{145}\text{Tm}$ , and  $E_p = 1.054(19)$  MeV in  $^{147}\text{Tm}$ . When compared with spherical WKB or DWBA calculations [37], the experimental half-lives for the two Tm isotopes are consistent with spectroscopic factors for decays from the  $h_{11/2}$  proton orbital. Though the predicted RHB ground-state configuration  $7/2^-[523]$  indeed originates from the spherical  $h_{11/2}$  orbital, the two nuclei are deformed.  $^{145}\text{Tm}$  has a prolate quadrupole deformation  $\beta_2 = 0.23$ , and  $^{147}\text{Tm}$  is oblate in the ground-state with  $\beta_2 = -0.19$ . Calculations also predict possible proton emitters  $^{136}\text{Tb}$  and  $^{135}\text{Tb}$  with separation energies  $-0.90$  MeV and  $-1.15$  MeV, respectively. In both isotopes the predicted ground-state proton configuration is  $3/2^+[411]$ .

The calculated mass quadrupole deformation parameters for the odd-Z nuclei  $59 \leq Z \leq 69$  at and beyond the drip-line are shown in Fig. 11. Pr, Pm, Eu and Tb isotopes are strongly prolate deformed ( $\beta_2 \approx 0.30 - 0.35$ ). By increasing the number of neutrons, Ho and Tm display a transition from prolate to oblate shapes. The absolute values of  $\beta_2$  decrease towards the spherical solutions at  $N = 82$ . The quadrupole deformations calculated in the RHB model with the NL3 effective interaction, are found in excellent agreement with the predictions of the macroscopic-microscopic mass model [38].

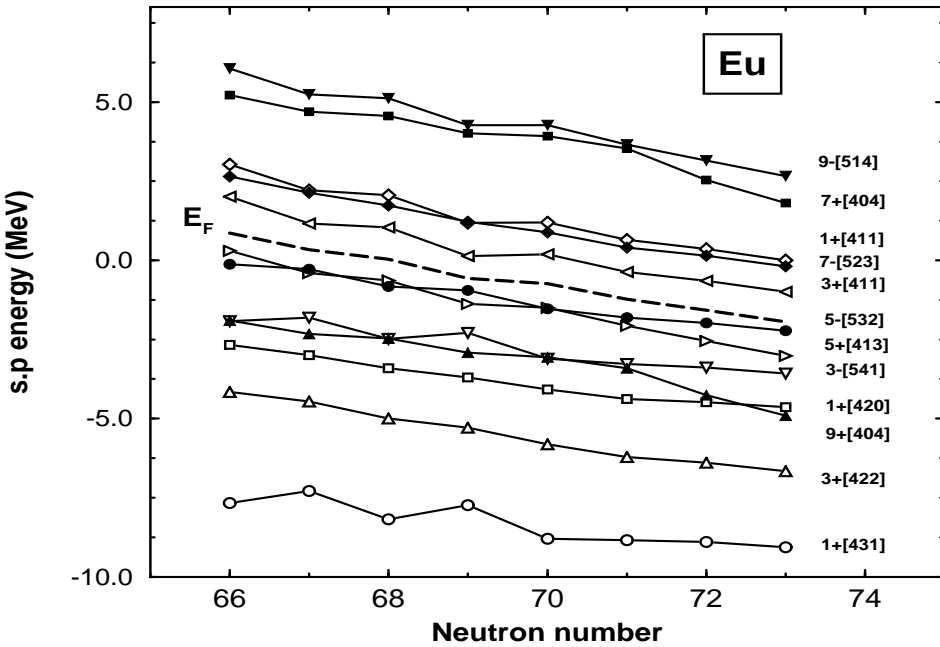


**FIGURE 12.** The proton single-particle levels for the Eu isotopes. The dashed line denotes the position of the Fermi level. The energies in the canonical basis correspond to ground-state solutions calculated with the NL3 effective force of the mean-field Lagrangian. The parameter set D1S is used for the finite range Gogny-type interaction in the pairing channel.

A detailed analysis of single proton levels, including spectroscopic factors, can be performed in the canonical basis which results from the fully microscopic and self-consistent RHB calculations. For the Eu isotopes this is illustrated in Fig. 12, where the proton single-particle energies in the canonical basis are shown as function of the neutron number. The thick dashed line denotes the position of the Fermi level. In particular, for the proton emitter  $^{131}\text{Eu}$ , the ground-state corresponds to the odd valence proton in the  $5/2^+[413]$  orbital.

## CONCLUSIONS

Models based on the relativistic mean-field approximation provide a microscopically consistent, and yet simple and economical treatment of the nuclear many-body problem. By adjusting just a few model parameters, coupling constants and effective masses, to global properties of simple, spherical and stable nuclei, it has been possible to describe in detail a variety of nuclear structure phenomena over the whole periodic table, from light nuclei to superheavy elements. When also pairing correlations are included in the self-consistent Hartree-Bogoliubov framework, the relativistic mean-field theory can be applied to the physics of exotic nuclei at the drip-lines. In the present review recent applications of the relativistic Hartree-Bogoliubov model have been described: description of the neutron drip-line in light nuclei, and of the microscopic mechanism for the formation of neutron halos;  $\Lambda$ -hypernuclei with large neutron excess; the study of the reduction of the effective spin-orbit interaction and the resulting modification of surface properties in drip-line nuclei; the suppression of shell effects and the onset of deformation and shape coexistence; the proton drip-line, and ground-state proton emitters in the region of deformed rare-earth nuclei.

The excellent results reported in these studies clearly reflect the basic advantages of the relativistic models over the more traditional non-relativistic approaches to nuclear structure: (i) models based on quantum hadrodynamics are more fundamental and they explicitly include mesonic degrees of freedom; (ii) they incorporate important relativistic effects, for instance the strong scalar and vector potentials and the resulting spin-orbit interaction. Of course, at the present stage, the most successful relativistic models are phenomenological. Although important results have been reported in the microscopic derivation of the low-energy hadronic Lagrangian, it is still not possible to bridge

the gap between QCD as the underlying theory of the strong interaction, and the effective theories that have to be used in the nuclear many-body problem. In applications to nuclear structure phenomena, one would also like to see a more consistent treatment of pairing correlations. The relativistic theory of pairing presents a very active area of research. However, only phenomenological effective forces have been shown to produce reliable results when applied to finite nuclei, especially in exotic regions. Important improvements should be expected also from models that include density dependent interactions and describe nucleons as composite objects. Particularly interesting are the extension of the RPA to the relativistic framework [39], and the time-dependent relativistic mean-field model [40,41], which can be used to describe excited collective states and analyze recent data on giant resonances at drip-lines. Large amplitude collective motion in exotic nuclei should also provide an excellent example for studies of the transition from regular to chaotic dynamics in quantum systems [42].

## REFERENCES

1. B.D. Serot and J.D. Walecka, *Adv. Nucl. Phys.* **16**, 1 (1986); *Int. J. Mod. Phys.* **E6**, 515 (1997).
2. P. Ring, *Progr. Part. Nucl. Phys.* **37**, 193 (1996).
3. Y.K. Gambhir, P. Ring, and A. Thimet, *Ann. Phys. (N.Y.)* **198**, 132 (1990).
4. J. Dobaczewski, W. Nazarewicz, T. R. Werner, J. F. Berger, C. R. Chinn, and J. Dechargé, *Phys. Rev. C* **53**, 2809 (1996).
5. H. Kucharek and P. Ring, *Z. Phys. A* **339**, 23 (1991).
6. W. Pöschl, D. Vretenar and P. Ring, *Comput. Phys. Commun.* **103**, 217 (1997).
7. W. Pöschl, D. Vretenar, G.A. Lalazissis, and P. Ring, *Phys. Rev. Lett.* **79**, 3841 (1997).
8. G.A. Lalazissis, D. Vretenar, W. Pöschl, and P. Ring, *Nucl. Phys. A* **632**, 363 (1998).
9. G.A. Lalazissis, D. Vretenar, W. Pöschl, and P. Ring, *Phys. Lett. B* **418**, 7 (1998).
10. D. Vretenar, W. Pöschl, G.A. Lalazissis, and P. Ring, *Phys. Rev. C* **57**, R1060 (1998).
11. T. Gonzalez-Llarena, J.L. Egido, G.A. Lalazissis, and P. Ring, *Phys. Lett. B* **379**, 13 (1996).
12. G.A. Lalazissis, D. Vretenar, and P. Ring, *Phys. Rev. C* **57**, 2294 (1998).
13. D. Vretenar, G.A. Lalazissis, and P. Ring, *Phys. Rev. C* **57**, 3071 (1998).
14. P.G. Reinhard, M.Rufa, J. Maruhn, W. Greiner and J. Friedrich, *Z. Phys. A* **323**, 13 (1986).
15. M.M. Sharma, M.A. Nagarajan, and P. Ring, *Phys. Lett. B* **312**, 377 (1993).
16. G.A. Lalazissis, J. König, and P. Ring, *Phys. Rev. C* **55**, 540 (1997).
17. J. F. Berger, M. Girod and D. Gogny, *Nucl. Phys. A* **428**, 32 (1984).
18. G. Audi and A. H. Wapstra, *Nucl. Phys. A* **595**, 409 (1995).
19. G.A. Lalazissis and P. Ring, *Phys. Lett. B* **427**, 225 (1998).
20. I. Tanihata et al., *Phys. Rev. Lett.* **55**, 2676 (1985); *Phys. Lett. B* **206**, 592 (1988).
21. I. Tanihata, *Prog. Part. Nucl. Phys.* **35**, 505 (1995).
22. P. Hansen, A.S. Jensen, and B. Jonson, *Annu. Rev. Nucl. Part. Phys.* **45**, 591 (1995).
23. J. Meng and P. Ring, *Phys. Rev. Lett.* **77**, 3963 (1996).
24. J. Meng and P. Ring, *Phys. Rev. Lett.* **80**, 460 (1998).
25. T. R. Werner, J. A. Sheikh, M.. Misu, W. Nazarewicz, J. Rikovska, K. Heeger, A. S. Umar and M. R. Strayer, *Nucl. Phys. A* **597**, 327 (1996).
26. G. A. Lalazissis, A. R. Farhan and M. M. Sharma, *Nucl. Phys. A* **628**, 221 (1998).
27. T. Glasmacher et al., *Phys. Lett. B* **395**, 163 (1997).
28. T. Glasmacher, *it Nucl. Phys. A* **630**, 278c (1998).
29. H. Scheit et al., *Phys. Rev. Lett.* **77**, 3967 (1996).
30. P.J. Woods and C.N. Davids, *Annu. Rev. Nucl. Part. Sci.* **47**, 541 (1997).
31. W. Nazarewicz, J. Dobaczewski, T. R. Werner, J. A. Maruhn, P.-G. Reinhard, K. Rutz, C. R. Chinn, A. S. Umar and M. R. Strayer, *Phys. Rev. C* **53**, 740 (1996).
32. W. E. Ormand, *Phys. Rev. C* **53**, 214 (1996).
33. B. Blank et al., *Phys. Rev. C* **50**, 2398 (1994).
34. C.N. Davids et al., *Phys. Rev. Lett.* **80**, 1849 (1998).
35. J.C. Batchelder et al., *Phys. Rev. C* **57**, R1042 (1998).
36. P.J. Sellin et al., *Phys. Rev. C* **47**, 1933 (1993).
37. S. Åberg, P.B. Semmes, and W. Nazarewicz, *Phys. Rev. C* **56**, 1762 (1997).
38. P. Möller, J.R. Nix, W.D. Myers, and W.J. Swiatecki, *At. Data Nucl. Data Tables* **59**, 185 (1995).
39. Z. Ma, N. Van Giai, and H. Toki, *Phys. Rev. C* **55**, 2385 (1997).
40. D. Vretenar, H. Berghammer, and P. Ring, *Nucl. Phys. A* **581**, 679 (1995).
41. D. Vretenar, G. A. Lalazissis, R. Behnsch, W. Pöschl and P. Ring, *Nucl. Phys. A* **621**, 853 (1997).
42. D. Vretenar, P. Ring, G. A. Lalazissis and W. Pöschl, *Phys. Rev. E* **56**, 6418 (1997).